Nanoscale

Dynamics of Carbohydrate Strands in Water and Interactions with Clay Minerals: Influence of pH, Surface Chemistry, and Electrolytes

Journal:	*Nanoscale*
Manuscript ID	NR-ART-03-2019-001867.R1
Article Type:	Paper
Date Submitted by the Author:	08-May-2019
Complete List of Authors:	Jamil, Tariq; University of Colorado-Boulder, Chemical and Biological Engineering; University of Colorado Gissinger, Jacob; University of Colorado-Boulder, Chemical and Biological Engineering Garley, Amanda; University of Colorado-Boulder, Chemical and Biological Engineering Saikia, Nabanita; University of Colorado-Boulder, Chemical and Biological Engineering Upadhyay, Arun; Procter and Gamble Co, PHC Heinz, Hendrik; University of Colorado-Boulder, Chemical and Biological Engineering

SCHOLARONE™
Manuscripts

Dynamics of Carbohydrate Strands in Water and Interactions with Clay Minerals: Influence of pH, Surface Chemistry, and Electrolytes

by

Tariq Jamil,[1] Jacob R. Gissinger,[2] Amanda Garley,[1] Nabanita Saikia,[1] Arun K. Upadhyay,[3]
Hendrik Heinz[1,2*]

[1] Department of Chemical and Biological Engineering, University of Colorado at Boulder, Boulder, CO 80309, USA

[2] Materials Science and Engineering Program, University of Colorado at Boulder, Boulder, CO 80309, USA

[3] The Procter & Gamble Company, Cincinnati, OH 45202, USA

* Corresponding author: hendrik.heinz@colorado.edu

Abstract

Carbohydrate hydrogels are extensively used in pharmaceuticals and engineered biomaterials. Molecular conformations, assembly, and interactions of the carbohydrate strands with stabilizers such as clay minerals in aqueous solution are difficult to quantify in experiments and the hydrogel properties remain largely a result of trial and error studies. We analyzed the assembly of gellan gum in aqueous solution and interactions with dispersed clay minerals in all-atomic detail using molecular dynamics simulation, atomic force microscopy (AFM), and comparisons to earlier measurements. Gellan strands associate at low pH values of 2 and gradually disassemble to double strands with weak association of -0.4 kcal per mole carbohydrate ring as the pH values increases to 9. Ionization of the carbonic acid side groups in the backbone extends the chains and accelerates the conformational dynamics via rapidly changing intramolecular ion bridges. Gellan interactions with clay minerals depend on the strength of electric triple layers between clay, cations, and anionic polymer strands, as well as weaker hydrogen bonds along the edges, which are tunable as a function of the clay surface chemistry, local ionic strength, pH values. Interaction energies range from -4 to +6 kcal per mol carbohydrate ring and were most favorable for electric triple layers with high charge mobility, which can be achieved for intermediate cation exchange capacity of the clay and high pH values to increase ionization of the clay edges and of the polymer. The findings provide understanding and help control the dynamics and stabilization of carbohydrate hydrogels by clay minerals.

Keywords: hydrogels; clay; interfaces; carbohydrates; molecular dynamics simulations

1. Introduction

Hydrogels play an important role in biology and medicine.[1] Bioengineered hydrogels are used for bone and cartilage repair,[2, 3] functional biomimetic skins,[4] therapeutics,[5] regulation of the fate and activity of stem cells upon stress relaxation,[6] as well as drug delivery.[7] Hydrogels consist of a network of hydrophilic polymers and can be assembled from a variety of organic compounds. Inorganic nanoparticles and double networks are often included to improve the mechanical stability.[8-11] Food-grade carbohydrate polymers[12-14] are often used for hydrogels in personal care and pharmaceutical products due to their effective thickening, emulsifying, and gelling properties.[15-20] Similarly, clay minerals[21-23] and layered double hydroxides have been employed to control hydrogel stability,[8, 9] swelling,[11] bending,[10] and rheological properties for 4D printing.[24]

Among the carbohydrates, gellan gum[25-27] is a microbial polysaccharide that forms a firm and transparent gel with advantageous properties such as heat-resistance in the presence of divalent cations and higher stability than other polysaccharide gels across a range of pH values, especially with high acyl content.[19, 20, 28, 29] Mechanisms of gelation have been extensively discussed,[16, 26, 30-33] however, interactions and assembly mechanisms at the molecular scale remain incompletely understood and the development of functional hydrogels relies extensively on trial-and-error experimentation.

The addition of clay minerals can strengthen hydrogel networks and control phase separation of dispersed active ingredients. In particular, smectite clays with solution-accessible cation densities in the range of 0.50 to 1.2 per nm^2 increase the viscosity and yield stress of electrolyte solutions[34, 35] and thereby improve the stability of immersed colloids.[23, 36-38] The chemistry of the clay minerals and polymers is often empirically chosen, however, and the magnitude of relevant interactions and the associated mechanisms are hardly known.

Atomistic and multiscale simulations have been able to overcome these limitations by providing missing insights down to the atomic scale.[39-41] In particular, the consistent representation of chemical bonding for inorganic and organic compounds, combined with the rigorous validation of structures and energies for a meaningful model Hamiltonian in the Interface force field (IFF) has reduced uncertainties in molecular simulations by a factor of ten.[42] Clay minerals were among the first compounds tested and facilitate quantitative explanations of aqueous and organic interactions.[35, 43-45] Computed binding energies and free energies typically deviate less than 10% from experiment,[46-48] and simulations using CHARMM-IFF have previously discovered molecular recognition mechanisms of peptides on nanoparticles,[46, 48-50, 61-62] explained specific crystal growth,[47, 51, 52] as well as catalytic activity at surfaces using reactive protocols.[53-56]

The purpose of this study is a systematic analysis of the interactions and assembly mechanisms of gellan gum-based hydrogels in aqueous solution with and without the presence of clay minerals using all-atom molecular dynamics simulation in combination with imaging by atomic force microscopy (AFM). The simulations overcome limitations in AFM imaging of the dissolved carbohydrates, which remains challenging in-situ and requires solvent removal. We examined the dynamics of multiple gellan strands in electrolyte solutions at different pH values and in contact with clay minerals for a range of compositions, including the first molecular models for veegum clay, a natural magnesium aluminum silicate[57] that is widely used in pharmaceutical formulations.[58-61]

2. Results and Discussion

2.1. Clay and Gellan Models. We prepared atomistic models for clay minerals of different composition from montmorillonite to high Mg veegum, including the first all-atom models for veegum clay based on elemental analysis and the classification as a dioctahedral smectite (Figure 1a-e, Table S1, and Section S1 in the Electronic Supplementary Information).[58] The composition of veegum clay is similar to montmorillonite (bentonite) with a mixed Na/Ca interlayer composition and higher Mg content in the octahedral layer (Table S1 in the Electronic Supplementary Information).[58-61] The lattice parameters are the same as for montmorillonite within 1% and the consensus stoichiometry of veegum HV (Type IC) is $Na_{0.33}Ca_{0.435}[Si_4O_8][Al_{0.80}Mg_{1.20}O_2(OH)_2]$. The remaining uncertainty in the relative composition of Na, Ca, Mg and (Al + Fe) is ±5% according to experiment, and we refer to this composition as "regular veegum" (Figure 1a-c). Models of veegum clay platelets of ~5 nm size were prepared for different pH values of 3.5 (Figure 1d) and 9 (Figure 1e), which differ in the protonation state of the silanol groups (SiOH) at the edges of the clay layer. Similar to silica surfaces, the Q^3 silanol edge groups (SiOH) ionize to $SiO^- \cdots Na^+$ groups by approximately 0%, 10%, and 25% at pH values of 3, 7, and 9, respectively.[50, 62] The acid-base chemistry of the aluminol groups (AlOH) at the edges also involves partial protonation of (AlOH) to $Al(OH_2)^+$ groups below pH ~ 4 and partial dissociation to $AlO^- \cdots Na^+$ groups above pH ~ 4. The stoichiometric ratio of AlOH to SiOH groups is only 1:5, however so that these equilibria could be neglected.

In addition to regular veegum clay, we employed models for veegum clay with lower Mg content, higher Mg content, and an acid-leached clay, as suggested in experiments (see Table S1 and Section S1 in the Electronic Supplementary Information).[63] Low Mg veegum was represented by montmorillonite with a cation exchange capacity (CEC) of 90 meq/100g,[42] high Mg veegum contained a 17.5% higher Mg content, and the leached veegum model equals a degraded composition after dissolution of 26% of the octahedral Mg^{2+} ions (present as $MgO(OH)^-$) and a corresponding stoichiometric amount of interlayer Na^+ and Ca^{2+} ions (Figure S1 in the Electronic Supplementary Information).[63] The leached ions were also removed from the surrounding solution.

Atomic charges, atom types, and force field parameters for molecular dynamics simulations of the clay minerals[42, 44] and the polymer interfaces were assigned according to the Interface force field (IFF).[42] IFF closely represents chemical bonding, lattice parameters within 1% of experiment, and surface energies within few percent of experimental data for clay minerals.[43-45, 49, 64-66]

Simulations of the aqueous interfaces of regular veegum clay show that 15-20% of Ca^{2+} interlayer ions and 15-20% of Na^+ interlayer ions dissociate more than 3 Å away from the clay surface atomic plane (see density profiles in Figure S2 in the Electronic Supplementary Information). The remaining 80-85% of cations remain bound to the surface. In addition, the migration of several Ca^{2+} ions from the interlayer into the octahedral sheet was observed (Figure 1c). The distribution of Ca^{2+} ions into the octahedral sheet has been suggested in experiments although it was not clearly observable.[58, 59]

Gellan gum consists of tetrasaccharide monomers which contain two glucose rings, glucuronic acid, and rhamnose (Figure 1f).[67, 68] We employed models of high-acyl gellan gum that is characterized by high pH stability and the chemical formula ([D-Glc(β1→4)D-GlcA(β1→4)D-Glc(β1→4)L-Rha(α1→3)]$_n$ with an average of 0.5 acyl and 1.0 sodium glycerate groups per monomer.[25] For this acyl content, we generated a repeat unit of 8 carbohydrate rings and utilized polymeric chains of 48 carbohydrate rings in all simulations (Figure 1f). The pH value predominantly affects the protonation state of the glucuronic acid groups in gellan gum, which have a pKa value of ~3.2,[69] while the remainder of gellan gum has no pH sensitivity in the range from 2 to 12. Accordingly, protonation states at pH ≤ 2, ~3.5, and ≥ 5 are represented by 0%, 50%, and 100% ionization of COOH groups to $COO^- \cdots Na^+$ in the D-GlcA units (Figure 1f). Zero, one, or two sodium glycerate groups were then present per repeat unit of 8 carbohydrate rings, respectively. The charges, atom types, and force field parameters correspond to the CHARMM36 force field. Large-scale molecular dynamics simulations of gellan and clay-gellan model systems of ~10 nm size were carried out in all-atom resolution using the CHARMM36-INTERFACE force field.[42]

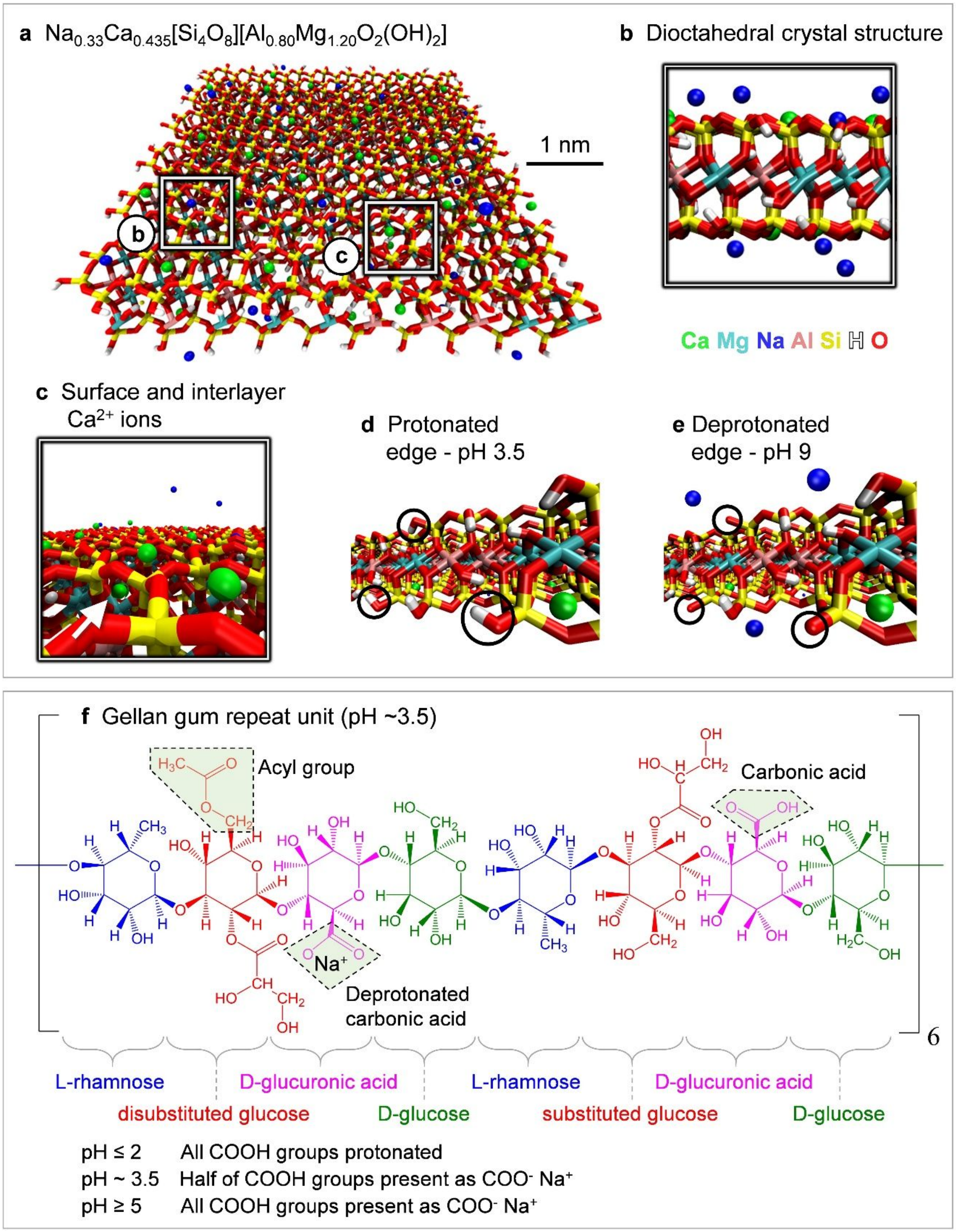

Figure 1. Structure of the main components in the hydrogel. (a) Model of a veegum clay platelet of 5×5×1 nm^3 size according to the average composition from elemental analysis (ref. [58]). (b) The dioctahedral structure of the inner AlOOH/MgOOH sheet of veegum clay, which can transition to

trioctahedral for higher Mg content (inset from a). (c) Ca^{2+} ions are tightly bound to the surface and sometimes located within the clay platelet according to the simulation (white arrow, inset from a). (d) At pH ~3.5, silanol groups Si-OH located at the edge of the clay nanoplatelet are fully protonated as known for silica surfaces (ref. [62]). (e) At pH ~9, 25% of silanol groups located at the edge of the clay nanoplatelet are deprotonated to siloxide groups ($SiO^{-} \cdots Na^{+}$) (ref. [62]). (f) Chemical structure of 48-ring gellan gum at pH ~3.5 with a repeat unit of 8 rings. At pH ≤ 2, all glucuronic acid units are protonated, whereas at ≥ pH 5 all are deprotonated.

2.2. Dynamics of Gellan Strands in Solution. Insights into the dynamics in aqueous solution was gained by relaxation of models of single, double, and triple strands of gellan gum without clay at pH values of 2, 3.5, and 9 (Figure 2a-d and Figures S3 to S5 in the Electronic Supplementary Information). The concentrations were ~1.7, ~3.3 and ~5.0 wt% in the simulation, resembling dilute solution and partly interacting gels.[67] Starting from a side-by-side position of the chains (Figure 2a), the strands showed some attraction at all pH values. At a pH value of 2, the strands remained in close contact with each other via intermolecular hydrogen bonds and an average distance of approximately 0.7 nm (Figures 2b, e, Table S2, and Figure S5 in the Electronic Supplementary Information). Hydrogen bonds between isolated strands had no particular order although stabilization of helical conformations reported in the solid state[70] appear feasible in case many more strands were present. At a pH value of 3.5, the strands partially disengaged with an average distance of ~1.5 nm between strands along the contour length (Figure 2c). The trend towards strand separation continued at pH values greater than 5 towards an average distance of ~2.2 nm (Figure 2d). The glucuronic acid groups were then partially or fully ionized, respectively, which leads to solvation of the anions and cations along the strands. The local hydration shells were the major driving force to move the strands apart. At the same time, positively charged Na^+ ions surrounded the negatively charged backbone at higher pH values and increased the time-average chain stiffness, represeted by the end-to-end length, from approximately 8.4 to 10.5 nm (Figure 2b-d). Despite such overall stiffening, the conformational flexibility of the polymer backbone increased significantly as intramolecular ion bridges ($COO^- \cdots Na^+ \cdots {}^-OOC$) rapidly rearranged and induced frequent temporary changes from extended to coiled conformations over the course of the simulation time of 100 ns. The distribution of end-to-end lengths widened and appears to be more bimodal at higher pH value than at low pH value (Figure S5 in the Electronic Supplementary Information). Hereby, shorter end-to-end lengths are associated with intramolecular salt bridges and larger end-to-end lengths with stiffer extended strands.

Sodium ions were found to coordinate carboxylate groups as well as oxygen atoms in hydroxyl groups, carbohydrate rings, acyl, and glycerate ester side groups pertaining to adjacent strands (Figure 2f and Figure S4e, f in the Electronic Supplementary Information). Therefore, the negative (favorable) interaction energy per strand increased upon ionization and was somewhat higher among triple strands compared to double strands at lower pH values (Figure 2g). The most significant increase occurred from pH 2 to 3.5. From pH 3.5 to pH 9 (for pH > 5) only little extra cohesion was added to double strands, and some lost for triple strands. On a per-ring basis for the 48-ring model polyelectrolytes, the interaction energy was approximately -0.1 kcal per mole carbohydrate ring at pH 2 and -0.35 kcal per mole carbohydrate ring at pH values greater than 3.5. An attraction is therefore present but it is smaller than the thermal energy of RT ~0.6 kcal/mol. Consistent with the preference toward strand separation at higher pH in the simulation (Figure 2a-d), Atomic Force Microscopy (AFM) images of dried gellan samples on mica substrates (upon solvent removal) indicate the same trend on a larger scale (Figure 2h-j). Decreasing association and increased branching of polymer chains occurs with increasing pH value from 2 to 9. The strands aggregate into thicker fibrils at pH 2 and are less aggregated at pH 9. The thickness (height) analysis in AFM indicates a fibril thickness between 1 and 2 nm at pH 2 that decreases to a fibril thickness between 0.5 and 1.0 nm at pH 9, whereby ~0.5 nm corresponds to single strands (Figure S7 in the Electronic Supplementary Information). Earlier AFM studies at near-neutral pH values also suggested approximately 0.5 to 1.0 nm thickness for gellan single strands and double-stranded helical structures.[71-73] A slight preference for double strands versus single strands or triple strands at neutral pH near 7 in the simulations (Figure 2g) also concurs with measurements of viscosity, refractive index, and dynamic light scattering.[74] The loose organization of gellan gum at higher pH values may reduce the number of junction zones (aggregates of multi-strand helices) and reduce the rigidity of the hydrogel at a larger scale.[27, 75]

The end-to-end lengths in the simulations have suggested an increase in stiffness with increasing pH values (Figure 2b-d). Somewhat folded and reoriented conformations were observed at low pH values and differ from fairly straight conformations at pH 9, given a limited contour length of 25 nm (Movies S1 to S4 in the Electronic Supplementary Information). The trends in the simulation compare qualitatively well with persistence lengths (L_p) of ~25 nm at low pH and much stiffer chains with a persistence length of ~96 nm at pH 9 according to the AFM data (Figure 2h-j). The AFM data also concur with earlier measurements of L_p ~ 98 nm near neutral pH values.[74]

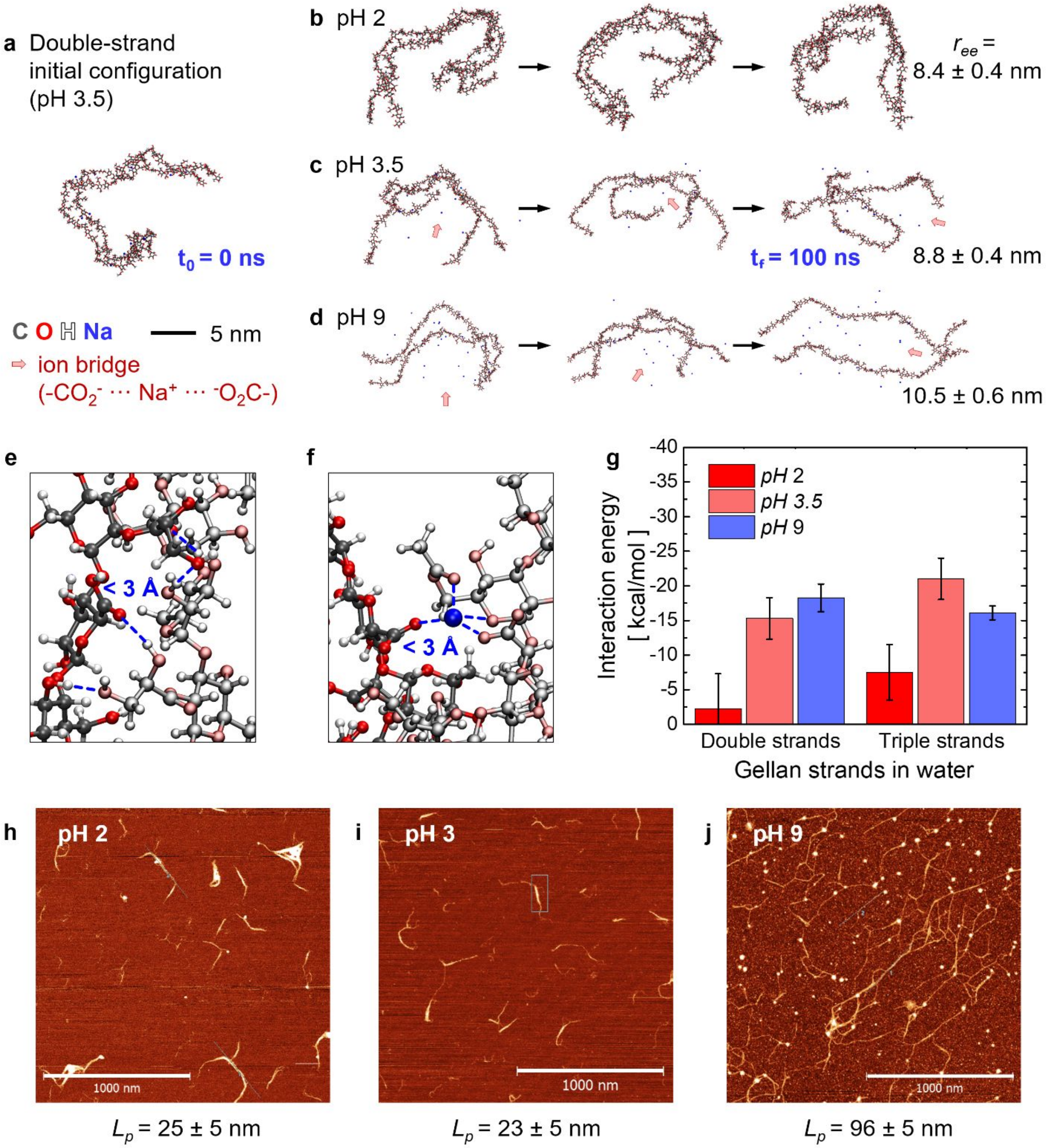

Figure 2. Dynamics of gellan gum as function of pH value in dilute aqueous solution according to molecular dynamics simulations and AFM images. (a) Initial conformation of gellan double strands in the simulation at pH 3.5. The contour length of the 48-ring gellan chains is 25.7 nm. (b-d) Representative conformations of double-strands of gellan over a simulation time of 100 ns

for pH values of 2, 3.5, and 9 (>5). pH values greater than 2 accelerate the dynamics between coiled and extended backbone states, introducing temporary folds stabilized by intramolecular ion bridges, while the average stiffness and end-to-end length increases. (e) Hydrogen bonds between gellan strands at pH = 2 lead to aggregation at close distance (blue highlights). (f) Ion bridges involving sodium ions, carboxylate groups, and complexation by other functional groups maintain favorable interactions between strands at pH = 3.5 and pH = 9. (g) Interaction energies between strands of gellan gum relative to relaxed single strands in solution, normalized per strand with 48 sugar rings. Interactions are more favorable for pH values >3.5 and stronger for triple strands (5.0 wt%) versus double strands (3.3 wt%) at pH values of 2. (h-j) AFM images of gellan gum on mica surfaces at pH values of 2, 3, and 9 after solvent evaporation. Persistence lengths and chain stiffness increase for higher pH values. Scale bars = 1000 nm. The *z* scale reaches up to ~ 3 nm (see height analysis in Figure S7 in the ESI).

2.3. Clay-Gellan Interactions. The addition of veegum clay attracts gellan gum and creates an interfacial region with increased ionic strength that stabilizes folded conformations of the chain (Figure 3). The models of the clay platelets were assumed to be of rectangular shape (Figure 3a-d) to approximate irregular and square-like shapes observed in AFM (Figure 3i, j). Ground clay platelets used for most purposes have irregular shapes[76-78] while crystal growth shows a preference towards pseudo-hexagonal shapes.[78, 79] The origin of platelet shape lies in the internal orientation of Si-O-Si and Al-O-Al bonds in the clay layer plane, which may favor growth along the (0 1 0), (1 1 0), and (1 -1 0) planes while cleavage energies are similar for many (h k l) surfaces and lead to irregular shapes upon grinding (Figure S6). The platelet shape has no major effect on the surface chemistry of the edges and polymer interactions,[79, 80] and our results do not depend on platelet geometry (see Section S2 in the Electronic Supplementary Information).

The overall strength of observed veegum-gellan interactions ranged from +4 to -6 kcal per mol carbohydrate ring depending on the aqueous conditions and the type of clay mineral (Figures 3 and 4). The interactions with the veegum surface are therefore more significant than gellan-gellan interactions in solution of only -0.4 kcal per mol carbohydrate ring (Figure 2). As previously shown for similar nanoparticle surfaces and polyeletrolytes, binding energies and binding free energies are effectively equal (within ±10%) as entropy losses of the polymer backbone upon binding are approximately offset by entropy gains upon release of surface-bound water.[47, 48, 51] Single strands were attracted to the regular veegum surface at an average distance between 1 and 3 nm from the top atomic layer at pH 3 and pH 9 (Figure 3a-d). The separation is larger than the closest possible approach of ~0.3 nm and indicates significant interactions with the electric double layer at the clay mineral surface. Contributions to the binding energy also arise from hydrogen bonds along the clay edges, which can persist over large fractions of simulation time (Figure 3e). In addition, ion pairing and salt bridges along ionic siloxide edge groups of the clay layer play a role in binding of gellan gum at pH 9 (Figure 3f). The primary interaction mechanism involves an electric triple layer (Figure 3g). The triple layer consists of ion pairs between the negatively charged clay basal plane and the dissociated cations from both the clay surface and the polymer backbone, as well as ion pairs between the positive charge in this layer with the negatively charged polymer backbone. The binding affinity of the polymer is largely created within this triple layer region between clay and polyelectrolyte, and increases in strength at higher pH value as the polymer and the clay edges become more ionic (Figure 3h). The addition of 10 mM sodium chloride to the solution had a moderating effect on adsorption, increasing the attraction of gellan gum from less than -1 kcal per mol carbohydrate ring to -3 kcal per mol carbohydrate ring at pH 3.5 while lowering the binding energy from -6 to -3 kcal per mol carbohydrate ring at pH 9 (Figure 3h).

The chain stiffness, represented by the root mean square end-to-end length, decreased from ~8.5 nm for freestanding gellan gum in solution to ~7 nm in the adsorbed conformation on veegum without much sensitivity to the pH value (Figure 3a, b). The addition of 10 mM salt had no effect on the chain stiffness in the bound state, however, it reduced the end-to-end length of gellan gum to ~8 nm and to only ~5 nm at pH 3.5 and 9 in solution, respectively (Figure 3c, d). These significant changes in conformation in solution were the result of added intramolecular ion bridges, especially at higher pH value and increased backbone ionization. At higher ionic strength, the polymers might ultimately aggregate (phase separate) and reduce the gel strength as observed in experiment.[26] The trends in the simulation are qualitatively supported by AFM images of the gellan-veegum gel after solvent removal (Figure 3i, j). Aggregation of gellan gum and some binding to the edges of clay platelets can be seen in AFM at pH 3 while a network of dispersed and bound chains is present at pH 8.

Insights from the AFM data are somewhat limited, however, as the images are recorded after solvent removal and some structural changes relative to the solution state have inevitably occurred. The thickness of the polymer strands is also difficult to distinguish from height histograms as the profile becomes fairly irregular in the presence of adsorbed clay particles (Figure S8 in the Electronic Supplementary Information). In principle, a Langmuir-type analysis of gellan binding to the clay surface could prove insightful for various gellan concentrations if very well-defined layer-like particles and in-situ AFM conditions would be used.[51] A well suited technique to characterize the interfaces are also zeta potential measurements,[81-83] which have shown an increase from approximately -50 mV for bare smectites in solution (cation exchange capacity of ~80 meq/100g) to zero and even positive values in the presence of alkylammonium ions in stoichiometric and in excess amounts, respectively.[82] Prior experiments have also shown a decrease in zeta potential at higher pH values,[83] which is qualitatively consistent with a higher density of dissociated cations near the surface and stronger gellan adsorption in the simulation (Figure 3d, h). Significant changes in zeta potentials upon addition of gellan gum to clay suspensions may be difficult to measure, however, as the concentration of gellan gum relative to clay is low in the dilute hydrogels (1/4th by weight, see methods in section 4.2), and only a small fraction of the polymer chains is in contact with the clay surface.

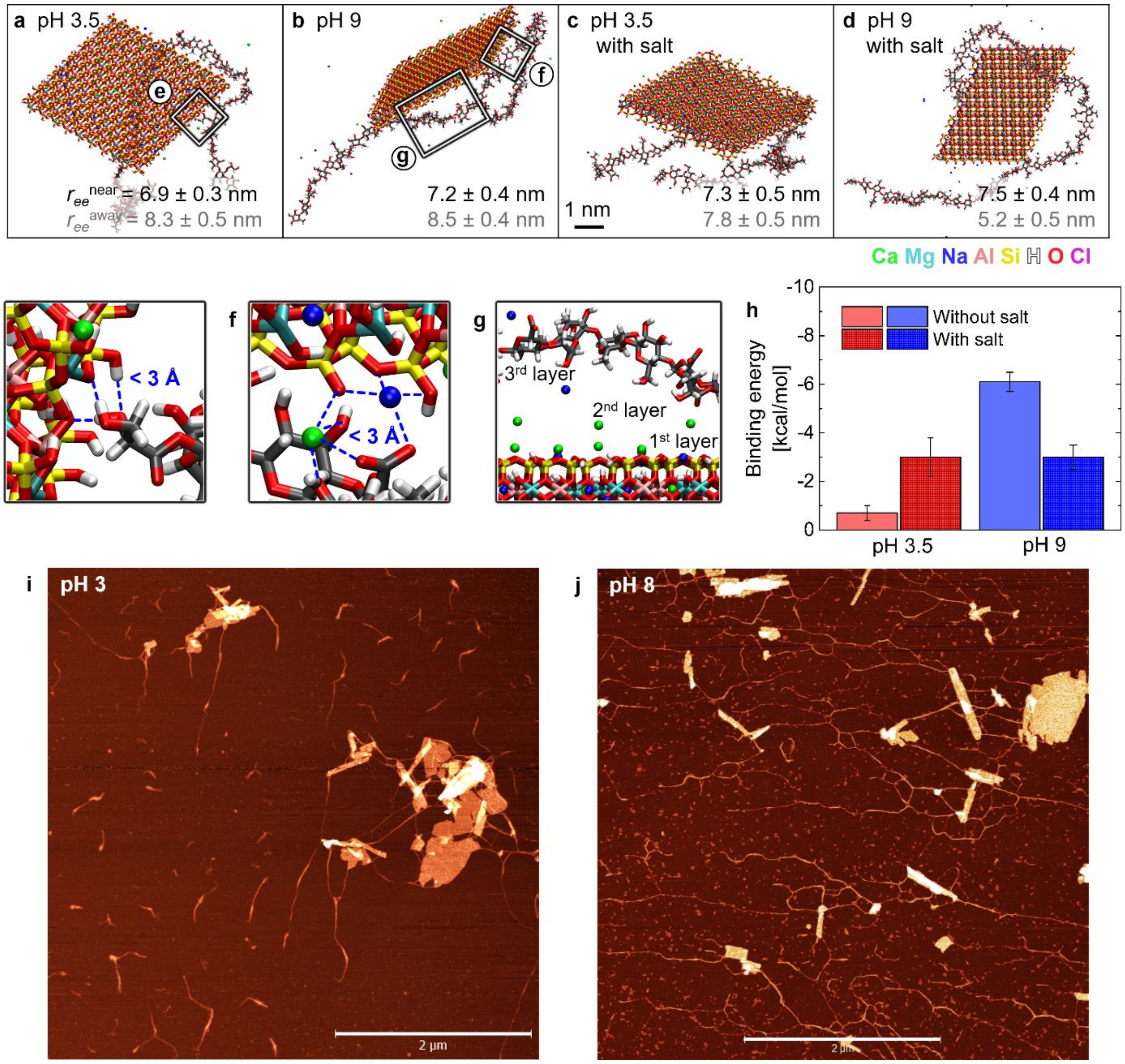

Figure 3. Interaction of gellan gum with regular veegum clay in dilute aqueous solution. The conditions are pH 3.5 and pH 9 with and without addition of ~10 mM NaCl. (a-d) Representative snapshots. At pH = 3.5, gellan gum tends to interact more with the edges of the clay platelet and less with the basal plane while the more ionic backbone at pH 9 assumes stronger interactions with the basal plane. The stiffness of gellan, represented by the end-to-end length r_{ee}, tends to be smaller near the surface than in solution except in (d) with higher overall ionic strength. Water molecules are not shown for clarity. (e) Hydrogen bonds between silanol groups (≡SiOH) and ≡Si-O-Si≡

bridges on clay edges with multiple functional groups in gellan gum. Si-O-Si bridges on the basal surface and ≡SiO$^-$ groups at edges at higher pH also form hydrogen bonds with gellan gum (not shown). (f) Formation of ion bridges between ≡SiO$^-$ groups on the clay edge, cations, and carboxylate groups in gellan gum at higher pH value. Ion complexation also involves uncharged groups (SiOH, ROH). (g) Significant binding of gellan gum to clay involves the formation of an electric triple layer between the negatively charged clay surface, dissociated cations from the clay surface and from the polymer backbone, and the negatively charged polymer backbone (-COO$^-$ groups). (h) Computed binding energy of gellan gum to veegum clay normalized per carbohydrate ring (48 rings per chain). (i, j) AFM images of veegum-gellan interactions at pH 3 and pH 8 after solvent removal. Better dispersion of strands and more favorable interactions with veegum are seen at pH 8. Scale bars = 2000 nm. The *z* scale reaches up to ~ 3 nm (see height analysis in Figure S8 in the ESI).

The affinity of gellan gum to veegum clay of lower Mg-content (montmorillonite) and the chain stiffness in the adsorbed state are similar to regular veegum clay at pH 3.5, even though uncertainties in the desorbed state are significant (Figure 4a, d and Table S3 in the Electronic Supplementary Information). The likely reason is a similar cation exchange capacity while the total area density of surface cations is reduced to only 30% (Table S1 in the Electronic Supplementary Information). High-Mg veegum, in contrast, leads to desorption of gellan gum (+4 kcal per mol carbohydrate ring) and the persistence length remains close to the value for single strands in dilute solution (Figure 4b, d). High Mg veegum has a higher area density of superficial Na^+ and Ca^{2+} ions, which enables less dissociation into the surrounding aqueous phase[62] and the superficial water layer is difficult to approach by gellan gum. The result are unfavorable ionic interactions and few hydrogen bonds. Veegum clay is also subject to partial ion exchange with hydronium ions and possible erosion of $Mg(OH)_2$ in the octahedral layer over extended periods of time (Figure S1 in the Electronic Supplementary Information). The regular veegum with some edge porosity has a similar, slightly larger negative binding energy of gellan gum of -1.2 kcal per mole carbohydrate ring at pH 3.5 (Figure 4c, d). Accordingly, such degradation does not affect polymer interactions much as the cation exchange capacity on the surface remains similar (Figure 4d). The gellan chain shows conformational flexibility and maintains contact with the leached clay, mostly via hydrogen bonds between hydroxyl groups and geminal silanol groups ($=Si(OH)_2$) at the edges of the leached platelet (Figure 4c). Binding of gellan gum to the basal plane was negligible and the end-to-end length decreased from ~10 nm to ~8 nm upon binding.

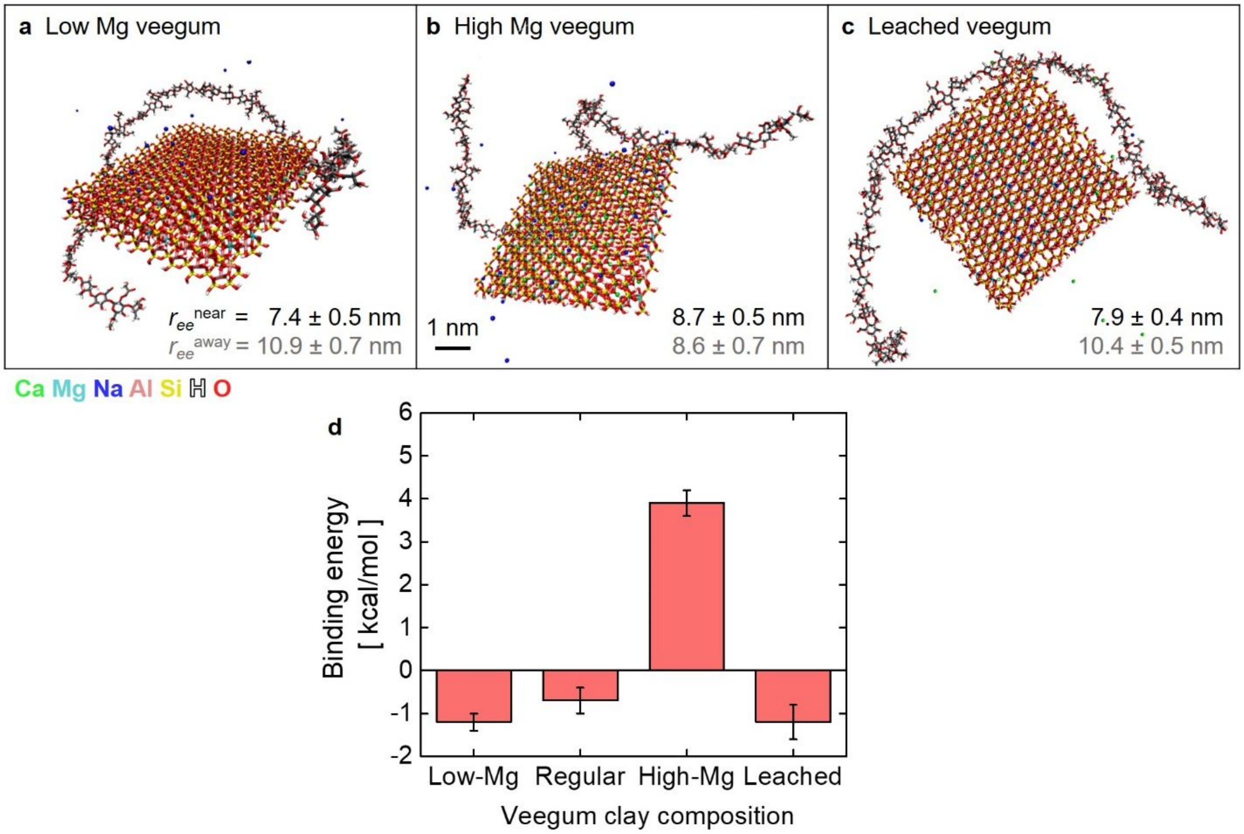

Figure 4. Interaction of gellan gum with different types of veegum clay at pH = 3.5. (a) Interaction with low-Mg veegum (montmorillonite). (b) Interaction with high-Mg veegum. The high area density of cations reduces dissociation into the aqueous phase and the surrounding hydration shells inhibit binding of gellan gum. (c) Interaction with leached veegum clay. A high fraction of surface-bound Ca^{2+} ions dissociates into solution and gellan gum adsorbs to geminal silanol groups at the edges via hydrogen bonds. (d) Binding energy of gellan gum to clay minerals of different composition, normalized per carbohydrate ring, including regular veegum for comparison.

2.4. Tuning the Magnitude of Clay-Gellan Binding. The simulations and available experimental data suggest that the electric triple layer consisting of the negatively charged clay surface, cations of clay and gellan, and the negatively charged gellan backbone plays a key role to explain the magnitude of clay-polymer binding (Figure 5). Gellan gum moves the cationic “cloud” surrounding the basal plane and the edge of the clay mineral closer to the clay surface, caused by its own cation density, especially when ionized at pH 3.5 and 9. Key parameters to rationalize the clay-carbohydrate interactions are the negative surface charge of the mineral (red), the amount of dissociated positive charge (blue), and the charge state of the polymer (orange/red) that can be controlled by the type of clay and solution pH (Figure 5). On montmorillonite (low Mg veegum) at pH 3.5, only sodium ions are present, the total surface charge is low, and cations dissociate several nanometers away from the surface (Figure 5a and Figure S2 in the Electronic Supplementary Information). The wide aqueous interfacial region enables strong attractive interactions with the negatively charged gellan strands (orange arrow in Figure 5a). Veegum clay has a three times higher surface charge, however, the fraction of dissociated cations is lower, and fewer ions dissociate several nanometers away from the surface (Figure 5b and Figure S2 in the

Electronic Supplementary Information). As a difference to montmorillonite, dissociated ions consist of divalent Ca^{2+} ions and monovalent Na^+ ions, of which the Ca^{2+} ions can form stronger ion bridges with gellan gum[17, 32] and lead to comparable gellan attraction (orange arrow in Figure 5b). High Mg veegum contains even more negative surface charge, related to the high Mg content in the inner octahedral sheet, and several surface Ca^{2+} ions are forced into the octahedral sheet, resulting in a mixed dioctahedral/trioctahedral clay structure (Figure 5c). The superficial hydration layers are more distinct and difficult to penetrate, further dissociated ions are mostly Na^+, and few ions travel more than a nanometer away from the clay layer (Figure S2 in the Electronic Supplementary Information). Gellan gum has no favorable interactions and is repelled when approaching closely (upward orange arrow in Figure 5c). An increase in pH to 9 on regular veegum surfaces dissociates more sodium and calcium ions due to the acidity of the silanol groups at the clay edges, and the polymer carries twice the charge compared to pH 3.5 (Figure 5d and Figure S2 in the Electronic Supplementary Information). The more ionic environment in the electric triple layer enables strong attraction of the polymer (orange arrow in Figure 5d).

In summary, the clay platelets act as cation donors and the local ionic strength determines the affinity to gellan. External changes in ionic strength such as salt addition also play a role and mainly affect the stability of the polymer in the desorbed state. Strongest clay-polymer interactions may be possible by enabling a wider triple layer region with high Ca^{2+} concentration, for example, using a Ca/Na bentonite clay with a surface charge between veegum and montmorillonite (Figure 5a, b) and a higher pH value to fully ionize the polymer backbone.

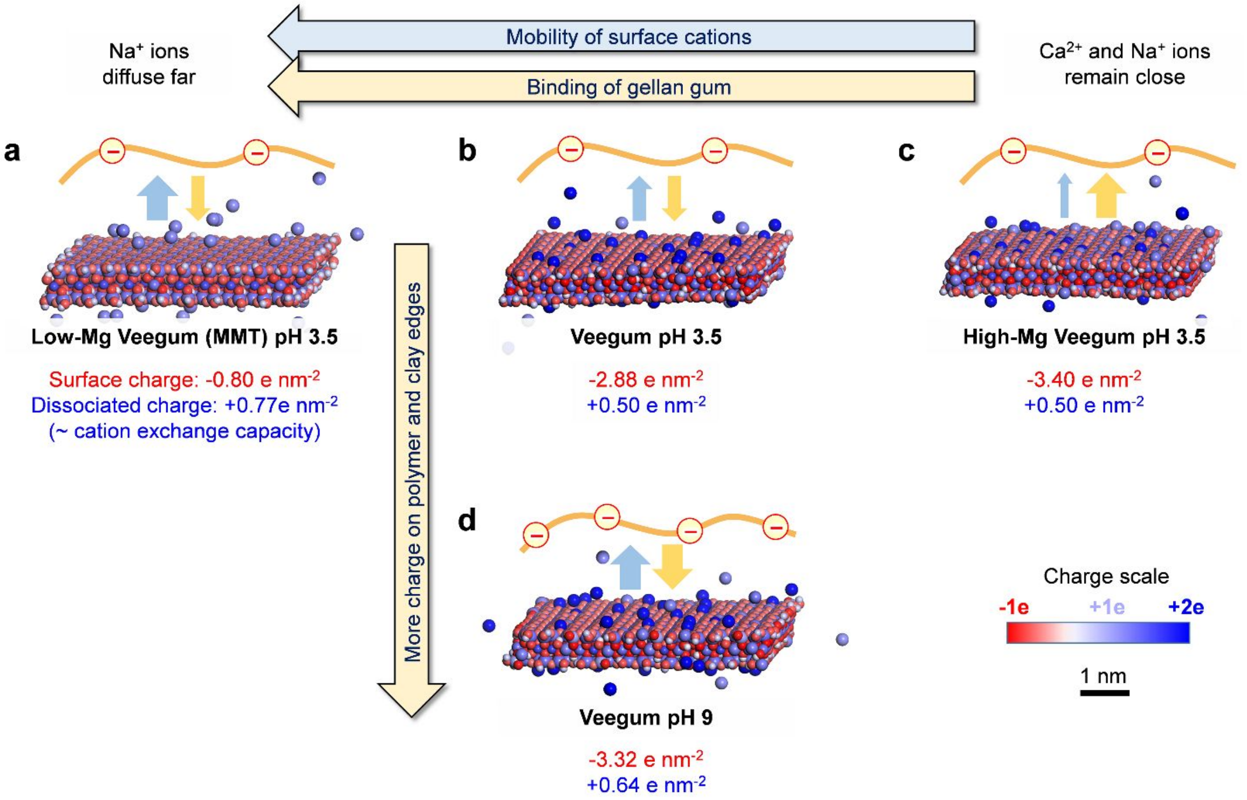

Figure 5. Relationship between clay-water interfaces and carbohydrate binding. Higher charge mobility in the electric triple layer enhances polymer adsorption. (a-c) The clay composition determines the total surface charge (red color), the amount of dissociated ions (blue color), and resulting polymer attraction via ion pairs and close contacts (orange arrows). High surface charge binds surface cations tightly and creates dense hydration layers that do no attract gellan gum. (d) At pH 9, more cations dissociate from the clay edges and the gellan backbone exhibits twice the number of ionic sites to interact with the clay mineral, leading to stronger binding.

3. Conclusions

We analyzed the assembly of gellan gum and the interaction with clay minerals as a function of surface chemistry, solution pH, and added electrolytes in atomic resolution using molecular dynamics simulation and AFM data. Prior insights at this scale were unavailable and we also introduced all-atom models for gellan gum and veegum clay minerals. Gellan strands tend to agglomerate at pH values below 3.5 and disassemble into loosely connected chains or double strands at pH values above 3.5 with a mild attraction of -0.4 kcal per mol carbohydrate ring. The polysaccharide backbone undergoes more rapid conformation equilibria between extended and coiled states when pH values increase from 2 to 5 or greater due to ionization and dynamic intramolecular ion bridges while the presence of a surrounding shell of ions increases the overall stiffness. The addition of veegum clay generates electric triple layers that can tune adsorption in a range of approximately ±5 kcal per mol carbohydrate ring depending on clay composition, pH, and added electrolytes. Edges of the clay platelets promote direct contact with gellan gum via hydrogen bonds whereas the basal plane generates ionic clouds into which gellan gum can enter and form stabilizing ion bridges. Strong clay-polymer attraction, increased conformational flexibility, and reduced chain stiffness is supported by intermediate clay surface charge and high mobility of interlayer cations, especially divalent ions, along with negatively charged gellan backbones and negatively charged clay edges at elevated pH values of 9.

The results provide design parameters for controlling the dynamics and stabilization of carbohydrate hydrogels in the presence of mineral modifiers that can benefit applications in personal care, drug delivery, and engineered biomaterials. The quantitative data and concepts are also useful to estimate rheological and mechanical properties up to the macroscale, which remains a difficult challenge for product formulations. The methods can be extended to other carbohydrate compositions, minerals, and pH conditions.

4. Methods

4.1. Computational Methods. New all-atom models of veegum clay platelets of 5×5×1 nm^3 size with different composition were developed based on data from X-ray diffraction, elemental analysis, and cation exchange capacity (Table S1, Section S1, and atomistic models supplied in the Electronic Supplementary Information).[58] The crystal structure is similar to montmorillonite and force field parameters were assigned according to the Interface force field (IFF) and the IFF surface model database.[42] The atomistic models are supplied in the Electronic Supplementary Information.

Atomistic models of high acyl gellan gum with a chain length of 48 carbohydrate rings were prepared using the CHARMM36 force field.[84] Parameters for specific functional groups and bond connectivity that are not supplied in CHARMM were assigned using atom equivalences and chemical analogy.

3D periodic models of approximately 10×10×10 nm^3 size were employed for the simulation of gellan assembly in solution with and without clay platelets. The systems contained 30,000 water molecules (TIP3P model), the chosen combination of gellan strands, clay platelet, and 6 formula units of NaCl as an added electrolyte (~10 mM). The volume of models of dilute polymer solutions with and without salt was set to match a density of 1000 kg/m^3. The volume of models of the clay-containing solutions was determined using additive molecular volumes of the solution phase with a density of 1000 kg/m^3 and of the clay platelets with a density of 2.60 g/cm^3.

The graphical user interface of Materials Studio was employed to prepare the models.[85] The models were then converted into .pdb./psf format (msi2namd) for NVT molecular dynamics simulations at 298.15 K with the CHARMM36-INTERFACE force field[42] and the NAMD program.[86] We carried out simulations with multiple replicas of 100 ns for each system using a time step of 1 fs, analyzed conformations and associated block average energies. The typical conformers include extended chains and locally bent chains due to ion bridges. Characteristic times for reforming ion bridges and changing conformations were on the order of 10 to 100 ns, and multiple concurrent simulations helped to ascertain the stated accuracy (Figures 2, 3, 4). Movies S1 to S8 provide 3D views of the dynamics.

The computation of binding energies involved two boxes of equal volume in the bound and unbound states.[87] Raw atomic coordinates over several hundred snapshots in equilibrium were processed into average ion density profiles, end-to-end lengths, radii of gyration, and persistence lengths. Full details of the development of the atomistic models (Section S1), shape of clay nanoplatelets (Section S2), computational methods (Section S3), atomistic models and force field files, as well as Movies S1 to S8 are provided in the Electronic Supplementary Information.

4.2. AFM Imaging of Gellan Gum and Gellan/Clay Interfaces. Aqueous stock solutions containing 0.025 wt% gellan gum and NaCl at a concentration of 1 mM were prepared by mixing the ingredients at high speed (~1000 rpm). HCl or NaOH were added to adjust the pH value to 2, 3, and 9, respectively, and the solution was incubated for 24-48 hours. Later the stock solutions were diluted 5-25 times to 0.001wt% - 0.005wt% with the same electrolyte of the same pH value. A 50 μL droplet of the solution was spin-coated at 2000 rpm for 2 min on a freshly cleaved mica surface. The surface of the coated sample was imaged with a Bruker's Dimension Icon atomic force microscope using ScanAsyst-Air probes (k=0.4 N/m).

Stock solutions containing 0.1 wt% veegum clay HV and 0.025 wt% gellan gum were prepared in the same fashion for pH values of 3 and 8. The solutions were diluted 5 times to 0.005wt% gellan and 0.02wt% veegum concentration. AFM images were obtained using the same protocol.

Acknowledgements

This work was supported by the National Science Foundation (CBET 1530790), Procter & Gamble, and the University of Colorado at Boulder. The allocation of computational resources at the CU Biofrontiers Computing Cluster and at the Ohio Supercomputing Center is acknowledged. This work used further resources at the Argonne Leadership Computing Facility, which is a DOE Office of Science User Facility supported under Contract DE-AC02-06CH11357, and the Janus supercomputer supported by the National Science Foundation (award number CNS-0821794). Discussions Ed Fitch and Dan White, Procter & Gamble, Masoud Sobani, University of Akron, and Hadi Ramezani-Dakhel, University of Chicago, are acknowledged.

References

1. N. A. Peppas, J. Z. Hilt, A. Khademhosseini and R. Langer, *Adv. Mater.*, 2006, **18**, 1345-1360.
2. D. A. Wang, S. Varghese, B. Sharma, I. Strehin, S. Fermanian, J. Gorham, D. H. Fairbrother, B. Cascio and J. H. Elisseeff, *Nat. Mater.*, 2007, **6**, 385-392.
3. J. R. Xavier, T. Thakur, P. Desai, M. K. Jaiswal, N. Sears, E. Cosgriff-Hernandez, R. Kaunas and A. K. Gaharwar, *Acs Nano*, 2015, **9**, 3109-3118.
4. C. Larson, B. Peele, S. Li, S. Robinson, M. Totaro, L. Beccai, B. Mazzolai and R. Shepherd, *Science*, 2016, **351**, 1071-1074.
5. R. T. Xing, K. Liu, T. F. Jiao, N. Zhang, K. Ma, R. Y. Zhang, Q. L. Zou, G. H. Ma and X. H. Yan, *Adv. Mater.*, 2016, **28**, 3669-3676.
6. O. Chaudhuri, L. Gu, D. Klumpers, M. Darnell, S. A. Bencherif, J. C. Weaver, N. Huebsch, H. P. Lee, E. Lippens, G. N. Duda and D. J. Mooney, *Nat. Mater.*, 2016, **15**, 326-334.
7. A. C. Anselmo and S. Mitragotri, *Adv. Drug Delivery Rev.*, 2017, **108**, 51-67.
8. G. R. Gao, G. L. Du, Y. J. Cheng and J. Fu, *J. Mater. Chem. B*, 2014, **2**, 1539-1548.
9. Z. Hu and G. Chen, *Adv. Mater.*, 2014, **26**, 5950-5956.
10. C. Yao, Z. Liu, C. Yang, W. Wang, X. J. Ju, R. Xie and L. Y. Chu, *Adv. Funct. Mater.*, 2015, **25**, 2980-2991.
11. Y. L. Ma, L. Lv, Y. R. Guo, Y. J. Fu, Q. Shao, T. T. Wu, S. J. Guo, K. Sun, X. K. Guo, E. K. Wujcik and Z. H. Guo, *Polymer*, 2017, **128**, 12-23.
12. G. O. Phillips and P. A. Williams, *Handbook of Hydrocolloids*, Elsevier Science, 2009.
13. P. Harris, *Food Gels*, Springer Netherlands, 2012.
14. M. Chaplin, *Hydrocolloids and gums*, http://www1.lsbu.ac.uk/water/water_structure_science.html.
15. A. S. D. Kołodyńska, B. e. Górecka, Z. Hubicki, *Emerging Concepts in Analysis and Applications of Hydrogels*, InTech, 2016.
16. T. Wüstenberg, *Cellulose and Cellulose Derivatives in the Food Industry: Fundamentals and Applications, First Edition. Weinheim: Wiley-VCH Verlag GmbH & Co. KGaA*, 2015, 1-68.
17. O. Kırtel, G. Avşar, B. A. Erkorkmaz and E. T. Öner, in *Microbial Production of Food Ingredients and Additives*, ed. A. M. Grumezescu, Academic Press, 2017, pp. 347-383.

18. A. M. Stephen and G. O. Phillips, *Food Polysaccharides and Their Applications*, CRC Press, 2016.
19. T. Osmałek, A. Froelich and S. Tasarek, *Int. J. Pharm.*, 2014, **466**, 328-340.
20. V. D. Prajapati, G. K. Jani, B. S. Zala and T. A. Khutliwala, *Carbohydr. Polym.*, 2013, **93**, 670-678.
21. F. Bergaya and G. Lagaly, *Handbook of Clay Science*, Elsevier, Amsterdam, 2013.
22. C. Aguzzi, P. Cerezo, C. Viseras and C. Caramella, *Appl. Clay Sci.*, 2007, **36**, 22-36.
23. C. Viseras, C. Aguzzi, P. Cerezo and A. Lopez-Galindo, *Appl. Clay Sci.*, 2007, **36**, 37-50.
24. A. S. Gladman, E. A. Matsumoto, R. G. Nuzzo, L. Mahadevan and J. A. Lewis, *Nat. Mater.*, 2016, **15**, 413-418.
25. P.-E. Jansson, B. Lindberg and P. A. Sandford, *Carbohydr. Res.*, 1983, **124**, 135-139.
26. E. R. Morris, K. Nishinari and M. Rinaudo, *Food Hydrocolloids*, 2012, **28**, 373-411.
27. D. Kang, H.-B. Zhang, Y. Nitta, Y.-P. Fang and K. Nishinari, in *Polysaccharides*, eds. K. Ramawat and J. M. Merillon, Springer, Cham, 2014, pp. 1-46.
28. J. F. Bradbeer, R. Hancocks, F. Spyropoulos and I. T. Norton, *Food hydrocolloids*, 2014, **35**, 522-530.
29. S. P. Denyer and R. M. Baird, *Guide to Microbiological Control in Pharmaceuticals and Medical Devices, Second Edition*, CRC Press, 2006.
30. K. Nishinari and R. Takahashi, *Curr. Opin. Colloid Interface Sci.*, 2003, **8**, 396-400.
31. O. Olatunji, *Natural Polymers: Industry Techniques and Applications*, Springer International Publishing, 2015.
32. M. Masakuni, *Adv. Biosci. Biotechnol.*, 2015, **6**, 22.
33. M. Tako, T. Teruya, Y. Tamaki and T. Konishi, *Colloid. Polym. Sci.*, 2009, **287**, 1445.
34. J. D. F. Ramsay and P. Lindner, *J. Chem. Soc. Faraday Trans.*, 1993, **89**, 4207-4214.
35. H. Heinz, *Clay Miner.*, 2012, **47**, 205-230.
36. S. Naficy, H. R. Brown, J. M. Razal, G. M. Spinks and P. G. Whitten, *Aust. J. Chem.*, 2011, **64**, 1007-1025.
37. R. Zafar, K. M. Zia, S. Tabasum, F. Jabeen, A. Noreen and M. Zuber, *Int. J. Biol. Macromol.*, 2016, **92**, 1012-1024.
38. L. Peña-Parás, J. A. Sánchez-Fernández and R. Vidaltamayo, in *Handbook of Ecomaterials*, eds. L. M. T. Martinez, O. V. Kharissova and B. I. Kharisov, Springer Nature, Cham, 2018.
39. H. Heinz and H. Ramezani-Dakhel, *Chem. Soc. Rev.*, 2016, **45**, 412-448.
40. Q. H. Zeng, A. B. Yu and G. Q. Lu, *Progr. Polym. Sci.*, 2008, **33**, 191-269.
41. R. K. Mishra, A. K. Mohamed, D. Geissbühler, H. Manzano, T. Jamil, R. Shahsavari, A. G. Kalinichev, S. Galmarini, L. Tao, H. Heinz, R. Pellenq, A. C. Van Duin, S. C. Parker, R. J. Flatt and P. Bowen, *Cem. Concr. Res.*, 2017, **102**, 68-89.
42. H. Heinz, T.-J. Lin, R. K. Mishra and F. S. Emami, *Langmuir*, 2013, **29**, 1754-1765.
43. Y. T. Fu, G. D. Zartman, M. Yoonessi, L. F. Drummy and H. Heinz, *J. Phys. Chem. C*, 2011, **115**, 22292-22300.
44. H. Heinz, H. Koerner, K. L. Anderson, R. A. Vaia and B. L. Farmer, *Chem. Mater.*, 2005, **17**, 5658-5669.
45. H. Heinz, H. J. Castelijns and U. W. Suter, *J. Am. Chem. Soc.*, 2003, **125**, 9500-9510.
46. I. L. Geada, H. Ramezani-Dakhel, T. Jamil, M. Sulpizi and H. Heinz, *Nat. Comm.*, 2018, **9**, 716.
47. H. Ramezani-Dakhel, L. Y. Ruan, Y. Huang and H. Heinz, *Adv. Funct. Mater.* , 2015, **25**, 1374-1384.
48. F. S. Emami, V. Puddu, R. J. Berry, V. Varshney, S. V. Patwardhan, C. C. Perry and H. Heinz, *Chem. Mater.*, 2014, **26**, 5725–5734.
49. H. Heinz, R. A. Vaia, R. Krishnamoorti and B. L. Farmer, *Chem. Mater.*, 2007, **19**, 59-68.
50. S. V. Patwardhan, F. S. Emami, R. J. Berry, S. E. Jones, R. R. Naik, O. Deschaume, H. Heinz and C. C. Perry, *J. Am. Chem. Soc.*, 2012, **134**, 6244-6256.

51. J. Chen, E. Zhu, J. Liu, S. Zhang, Z. Lin, X. Duan, H. Heinz, Y. Huang and J. J. D. Yoreo, *Science*, 2018, **362**, 1135-1139.
52. L. Ruan, H. Ramezani-Dakhel, C.-Y. Chiu, E. Zhu, Y. Li, H. Heinz and Y. Huang, *Nano Lett.*, 2013, **13**, 840-846.
53. H. Ramezani-Dakhel, P. A. Mirau, R. R. Naik, M. R. Knecht and H. Heinz, *Phys. Chem. Chem. Phys.*, 2013, **15**, 5488-5492.
54. H. Ramezani-Dakhel, N. M. Bedford, T. J. Woehl, M. R. Knecht, R. R. Naik and H. Heinz, *Nanoscale*, 2017, **9**, 8401-8409.
55. B. Briggs, N. M. Bedford, S. Seifert, H. Koerner, H. Ramezani-Dakhel, H. Heinz, R. R. Naik, A. Frenkel and M. R. Knecht, *Chem. Sci.*, 2015, **6**, 6413-6419.
56. N. M. Bedford, H. Ramezani-Dakhel, J. M. Slocik, B. D. Briggs, Y. Ren, A. I. Frenkel, V. Petkov, H. Heinz, R. R. Naik and M. R. Knecht, *Acs Nano*, 2015, **9**, 5082-5092.
57. *Magnesium Aluminum Silicate*, U. S. Pharmacopoeia, Rockville, MD, 2011, vol. NF 30, pp. 1845-1847.
58. K. P. Lee, *The Flocculation of Veegum Suspension by Electrolytes*, University of Utah, PhD Thesis, Salt Lake City, 1969.
59. H. Vogt, *Die Pharmazeutische Industrie*, 1963, **25**, 12-15.
60. P. L. Kwang, C. M. Robert and T. Ree, *J. Korean Chem. Soc.*, 1972, **16**, 25-32.
61. *VEEGUM Magnesium Aluminum Silicate*, Vanderbilt Minerals LLC, Norwalk, CT, 2018.
62. F. S. Emami, V. Puddu, R. J. Berry, V. Varshney, S. V. Patwardhan, C. C. Perry and H. Heinz, *Chem. Mater.*, 2014, **26**, 2647-2658.
63. D. W. Thompson and J. T. Butterworth, *J. Colloid Interface Sci.*, 1992, **151**, 236-243.
64. H. Heinz and U. W. Suter, *Angew. Chem., Int. Ed.*, 2004, **43**, 2239-2243.
65. H. Heinz, R. A. Vaia, H. Koerner and B. L. Farmer, *Chem. Mater.*, 2008, **20**, 6444-6456.
66. H. Heinz, R. A. Vaia and B. L. Farmer, *J. Chem. Phys.*, 2006, **124**, 224713.
67. E. Miyoshi, T. Takaya and K. Nishinari, *Food hydrocolloids*, 1994, **8**, 505-527.
68. K. Nishinari, *Physical Chemistry and Industrial Application of Gellan Gum*, Springer Berlin Heidelberg, 2003.
69. R. Kohn and P. Kovac, *Chem. Zvesti*, 1978, **32**, 478-485.
70. C. Upstill, E. D. T. Atkins and P. T. Attwool, *Int. J. Biol. Macromol.*, 1986, **8**, 275-288.
71. S. Ikeda, S. Gohtani, K. Nishinari and Q. Zhong, *Food Sci. Technol. Res.*, 2013, **19**, 201-210.
72. T. Funami, S. Noda, M. Nakauma, S. Ishihara, R. Takahashi, S. Al-Assaf, S. Ikeda, K. Nishinari and G. O. Phillips, *J. Agric. Food Chem.*, 2008, **56**, 8609-8618.
73. T. Funami, S. Noda, M. Nakauma, S. Ishihara, R. Takahashi, S. Al-Assaf, S. Ikeda, K. Nishinari and G. O. Phillips, *Food Hydrocolloids*, 2009, **23**, 548-554.
74. R. Takahashi, H. Tokunou, K. Kubota, E. Ogawa, T. Oida, T. Kawase and K. Nishinari, *Biomacromolecules*, 2004, **5**, 516-523.
75. C. S. F. Picone and R. L. Cunha, *Carbohydr. Polym.*, 2011, **84**, 662-668.
76. T. T. T. Ho, Y. S. Ko, T. Zimmermann, T. Geiger and W. Caseri, *J. Mater. Sci.*, 2012, **47**, 4370-4382.
77. R. H. A. Ras, Y. Umemura, C. T. Johnston, A. Yamagishi and R. A. Schoonheydt, *Phys. Chem. Chem. Phys.*, 2007, **9**, 918-932.
78. P. H. Nadeau, *Clay Miner.*, 1985, **20**, 499-514.
79. T. A. Ho, J. A. Greathouse, A. S. Lee and L. J. Criscenti, *Langmuir*, 2018, **34**, 5926-5934.
80. X. Liu, X. Lu, Y. Zhang, C. Zhang and R. Wang, *Phys. Chem. Chem. Phys.*, 2017, **19**, 18400-18406.
81. M. Chorom and P. Rengasamy, *Eur. J. Soil Sci.*, 1995, **46**, 657-665.
82. D. Zadaka, A. Radian and Y. G. Mishael, *J. Colloid Interface Sci.*, 2010, **352**, 171-177.
83. E. M. Pecini and M. J. Avena, *Langmuir*, 2013, **29**, 14926-14934.
84. J. Huang and A. D. MacKerell Jr, *J. Comput. Chem.*, 2013, **34**, 2135-2145.

85. *Materials Studio 2019 Program Suite and User Guide*, Biovia/Dassault Systemes, Cambridge, UK, 2019.
86. J. C. Phillips, R. Braun, W. Wang, J. Gumbart, E. Tajkhorshid, E. Villa, C. Chipot, R. D. Skeel, L. Kale and K. Schulten, *J. Comput. Chem.*, 2005, **26**, 1781-1802.
87. Y. T. Fu and H. Heinz, *Chem. Mater.*, 2010, **22**, 1595-1605.

Table of Contents Entry

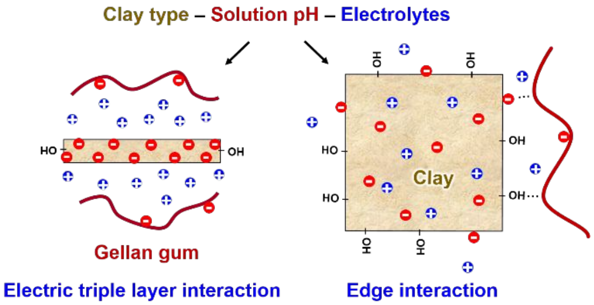

We describe the dynamics of gellan strands in solution and design principles to tune the attraction to clay platelets.